


Controlling the stability of nonlinear optical modes via electromagnetically induced transparency

Kun Zhang, Yi-zeng Liang, Ji Lin, and Hui-jun Li*

Institute of Nonlinear Physics and Department of Physics, Zhejiang Normal University, Jinhua, 321004 Zhejiang, China (Received 24 July 2017; revised manuscript received 28 November 2017; published 27 February 2018)

We propose a scheme to generate and stabilize the high-dimensional spatial solitons via electromagnetically induced transparency (EIT). The system we consider is a resonant atomic ensemble having Λ configuration. We illustrate that under EIT conditions the equation satisfied by the probe field envelope is reduced to a saturable nonlinear Schrödinger equation with the trapping potential, provided by a far-detuned laser field and a random magnetic field. We present high-dimensional soliton solutions exhibiting many interesting characteristics, including diversity (i.e., many different types of soliton solutions can be found, including bright, ring multipole bright, ring multipole defect mode, multiring bright, multiring defect mode, and vortices solitons), the phase transition between bright soliton and higher-order defect modes (i.e., the phase transition can be realized by controlling the nonlinear coefficient or the intensity of the trapping potential), and stability (i.e., various solitons can be stabilized by the Gaussian potential provided by the far detuned laser field, or the random potential provided by the magnetic field). We also find that some solitons are the extension of the linear eigenmode, whereas others entirely derive from the role of nonlinearity. Compared with previous studies, we not only show the diverse soliton solutions in the same system but also find the boundary of the phase transition for the type of solitons. In addition, we present the possibility of using the random potential to stabilize various solitons and vortices.

DOI: [10.1103/PhysRevA.97.023844](https://doi.org/10.1103/PhysRevA.97.023844)**I. INTRODUCTION**

Spatial optical solitons are special wave packets resulting from the interaction between diffraction and nonlinearity. Their rich nonlinear physics and important practical applications [1–5] have attracted a lot of attention among researchers. However, in order to avoid significant optical absorption, a very high light intensity is used to obtain enough nonlinearity for balancing the diffraction effect via passive optical media.

Recently, there has been much interest in highly resonant media via electromagnetically induced transparency (EIT) [6], in which many striking characteristics—including the suppression of optical absorption [7], a large reduction of group velocity [8], a giant enhancement of Kerr nonlinearity with very low power light field [9], and many adjustable parameters such as field intensity, detuning, and atomic density—have been discussed. Thus, much research—including ultraslow optical transmission and storage [10,11], phase gates [12], optical clocks [13], efficient four-wave mixing [14], bistable states [15], and high-dimensional spatiotemporal optical solitons [16]—has been reported. In addition, due to the similarity between the light field transmission equation and the quantum Schrödinger equation, the EIT system is also used to simulate some quantum systems [17], such as the Anderson model [18,19], the parity-time symmetrical model [20–24], and the Thirring model [25].

There have been discussions of the (2+1)-dimensional [(2+1)D] saturable nonlinear Schrödinger equation (SNLSE) [26,27] (or the cubic-quintic nonlinear Schrödinger equation [28]) and its related soliton solutions in coherent atomic media.

Bright ground solitons, vortices [29,30], and double-hump solitons (the amplitude functions of which cross zero once) [31] have been found in the (2+1)D SNLSE, and lattice solitons [32] and discrete solitons [33] have also been found in the SNLSE in which there was the periodical modulation potential in the denominator of the saturable nonlinear term. However, the linear-type multipole solitons, the ring-type multipole solitons, and the higher-order defect mode are not found. Except for the bright ground solitons and lattice solitons [32], all others solitons are unstable. Thus, it is important to generate and stabilize these high-dimensional nonlinear solutions for the SNLSE.

In this paper, we propose a scheme to generate and stabilize high-dimensional spatial solitons via EIT. The system we consider is a cold, resonant atomic scheme having Λ -type level configuration and interacting with a probe, control, far-detuned laser, and magnetic field. The resonant atomic scheme having Λ -type level configuration and interacting with a probe and control field has been used to construct the SNLSE [26], but we introduce the potential generated by the ac Stark and Zeeman effects for generating stable and diverse solitons. We show that under some conditions the envelope equation of the probe field can be reduced into a (2+1)D SNLSE with the trapping potential formed by the far-detuned static laser field and the random magnetic field. A similar nonlinearity has been studied in [32,34–38] based on the biased photorefractive crystal [39]. Lattice solitons [32], defect solitons [35,37], interface kink solitons [36], and surface lattice solitons [38] have been discussed. However, all the optical lattice potentials are in the denominator of the saturable nonlinear term except for the model in [36]. Additionally, except for the model in [32], all the models discussed are in the (1+1) dimension. However, in our model, not only are various soliton solutions

*hjli@zjnu.cn

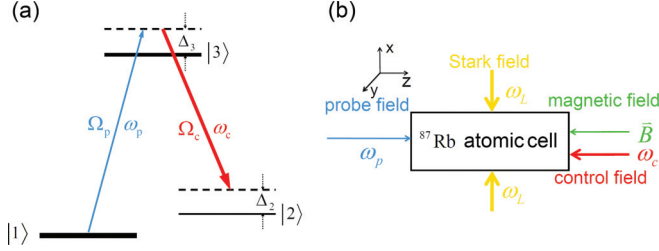


FIG. 1. (a) Excitation scheme of the lifetime broadened three-state atomic system interacting with a weak probe field with the half Rabi frequency Ω_p , and a strong continuous-wave control field with the half Rabi frequency Ω_c . (b) Possible experimental arrangement of the laser and magnetic fields.

such as ground solitons, multipole solitons, higher-order defect modes, and vortices found, but also they are stable. In addition, we can control the phase transition between bright solitons and higher-order defect modes by the nonlinear coefficient or the intensity of the trapping potential. We demonstrate that the system can be used to not only find and stabilize various high-dimensional soliton solutions but also display the feasibility of the phase transition from the bright solitons to the higher-order defect modes.

The paper is arranged as follows. In the next section, we give an introduction of the model under study. In Sec. III, we derive the nonlinear equations for the envelope of the probe field, which can be reduced to a (2+1)D SNLSE. In Sec. IV, the properties and stability of various solitons are shown. In the final section, we summarize the main results obtained in our paper.

II. MODEL AND EQUATIONS OF MOTION

A. Model

We consider a lifetime-broadened atomic system with a Λ -type energy-level configuration, as shown in Fig. 1. A weak probe field $\mathbf{E}_p = \mathbf{e}_x \mathcal{E}_p(x, y, z, t) \exp[i(k_p z - \omega_p t)] + \text{c.c.}$ and a strong control field $\mathbf{E}_c = \mathbf{e}_x \mathcal{E}_c \exp[i(-k_c z - \omega_c t)] + \text{c.c.}$ interact resonantly with levels $|1\rangle \rightarrow |3\rangle$ and $|2\rangle \rightarrow |3\rangle$, respectively. Here \mathbf{e}_j , k_j , and \mathcal{E}_j are, respectively, the polarization unit vector in the j th direction, the wave number, and the envelope of the j th field. The levels $|l\rangle$ ($l = 1, 2, 3$) together with \mathbf{E}_p and \mathbf{E}_c constitute a well-known Λ -type EIT core in which the absorption of the probe field is suppressed due to the quantum interference effect induced by the control field.

Furthermore, we assume that a far-detuned (Stark) optical lattice field

$$\mathbf{E}_{\text{Stark}} = \mathbf{e}_y \sqrt{2} E_0(x, y) \cos(\omega_L t) \quad (1)$$

is applied to the system, where E_0 and ω_L are, respectively, the field amplitude and angular frequency. Due to the existence of $\mathbf{E}_{\text{Stark}}$, a small Stark shift of level E_j to the state $|j\rangle$ occurs in the transverse direction, i.e., $E_j \rightarrow E_j + \Delta E_j$ with $\Delta E_j = -\frac{1}{2} \alpha_j \langle \mathbf{E}_{\text{Stark}}^2 \rangle_t = -\frac{1}{2} \alpha_j E_0^2(x, y)$, where α_j is the scalar polarizability of the level $|j\rangle$, and $\langle \dots \rangle_t$ denotes the time average in an oscillating cycle.

In addition, we assume that another random weak magnetic field

$$\mathbf{B}(x, y) = \mathbf{e}_y B_1(x, y) \quad (2)$$

is added to the system, where $B_1(x, y)$ is a random distribution magnetic field along the transverse direction, which will contribute to a small random Zeeman level shift $\Delta E_{\text{Zeeman}} = \mu_B g_F^j m_F^j B_1(x, y) = \mu_j B_1(x, y)$. Such a random magnetic field can be realized by adding a demagnetized neodymium-iron-boron ferromagnet [40].

As will be shown below, the Stark shift contributed by the far-detuned Stark field $\mathbf{E}_{\text{Stark}}$ given by Eq. (1) and the Zeeman level shift contributed by the magnetic field \mathbf{B} given by Eq. (2) will provide the refractive index to the probe field. Additionally, the form of the refractive index will be decided by the spatial distribution of the Stark field and magnetic field. In Fig. 1(a), $\Omega_p = (\mathbf{e}_x \cdot \mathbf{p}_{13}) \mathcal{E}_p / \hbar$ and $\Omega_c = (\mathbf{e}_x \cdot \mathbf{p}_{23}) \mathcal{E}_c / \hbar$ are, respectively, the half Rabi frequencies of the probe and control fields, where \mathbf{p}_{ij} signifies the electric dipole matrix element of the transition from state $|i\rangle$ to $|j\rangle$, and Δ_3 and Δ_2 are, respectively, one- and two-photon detunings in the relevant transitions. Figure 1(b) shows a possible experimental arrangement.

B. Maxwell-Schrödinger equations

Under electric dipole and rotating-wave approximations, the Hamiltonian of the system in the interaction picture reads $\hat{H}_{\text{int}} = -\hbar \sum_{j=1}^3 \Delta'_j |j\rangle \langle j| - \hbar (\Omega_p |3\rangle \langle 1| + \Omega_c |3\rangle \langle 2| + \text{H.c.})$, where H.c. denotes the Hermitian conjugate, and

$$\Delta'_j = \Delta_j + \frac{\alpha_j}{2\hbar} |E_0(x, y)|^2 - \frac{\mu_j}{\hbar} B_1(x, y). \quad (3)$$

The motion of atoms interacting with the light field is described by the Schrödinger equation

$$\left(i \frac{\partial}{\partial t} + d'_2 \right) a_2 + \Omega_c^* a_3 = 0, \quad (4a)$$

$$\left(i \frac{\partial}{\partial t} + d'_3 \right) a_3 + \Omega_p a_1 + \Omega_c a_2 = 0, \quad (4b)$$

with $\sum_{j=1}^3 |a_j|^2 = 1$ and $d'_j = \Delta'_j + i\gamma_j = d_j + \frac{\alpha_j}{2\hbar} |E_0(x, y)|^2 - \frac{\mu_j}{\hbar} B_1(x, y)$, where a_j and γ_j are the probability amplitude and the decay rate of the states $|j\rangle$ ($j = 2, 3$).

Under a slowly varying envelope approximation, the Maxwell equation of the probe field is reduced to

$$i \left(\frac{\partial}{\partial z} + \frac{1}{c} \frac{\partial}{\partial t} \right) \Omega_p + \frac{c}{2\omega_p} \left(\frac{\partial^2}{\partial x^2} + \frac{\partial^2}{\partial y^2} \right) \Omega_p + \kappa_{13} a_3 a_1^* = 0, \quad (5)$$

where $\kappa_{13} = N \omega_p |\mathbf{e}_x \cdot \mathbf{p}_{13}|^2 / (2\epsilon_0 \hbar c)$ with N being the atomic concentration.

III. (2+1)D NONLINEAR ENVELOPE EQUATION FOR THE PROBE FIELD

We focus on the steady-state regime of the system, in which time-derivative terms in Eqs. (4) and (5) can be neglected.

Such a regime can be realized by using the probe field with a large time length (i.e., $|d_j|\tau_0 \gg 1$, where τ_0 is the pulse length of the probe field) and hence the response of atoms can follow the variation of the probe field adiabatically. The solutions of Eq. (4) are acquired as $a_3 = d'_2\Omega_p a_1/D'$ and $a_2 = -\Omega_c^*\Omega_p a_1/D'$, with $|a_1|^2 = \frac{1}{1+W|\Omega_p|^2}$, $W' = (|\Omega_c|^2 + |d'_2|^2)/|D'|^2$, and $D' = |\Omega_c|^2 - d'_2 d'_3$.

In general, we consider that the probe field is weaker than the control field, and the Stark and Zeeman energy shifts are smaller than the detuning Δ_j . After some simple calculations, and neglecting the higher-order terms, Eq. (5) is reduced into the (2+1)D equation with saturable nonlinearity and trapping potential:

$$i\frac{\partial\Omega_p}{\partial z} + \frac{c}{2\omega_p}\nabla_{\perp}^2\Omega_p + \frac{\kappa_{13}d_2}{D}\frac{\Omega_p}{1+W|\Omega_p|^2} + \alpha|E_0(x,y)|^2\Omega_p + \beta B_1(x,y)\Omega_p = 0, \quad (6)$$

with $\alpha = \kappa_{13}[\alpha_2 D + d_2(\alpha_2 d_3 + \alpha_3 d_2)]/(2\hbar D^2)$, $\beta = \kappa_{13}[\mu_2 D + d_2(\mu_2 d_3 + \mu_3 d_2)]/(\hbar D^2)$, $W = (|\Omega_c|^2 + |d_2|^2)/|D|^2$, and $D = |\Omega_c|^2 - d_2 d_3$. Equation (6) can be written into the dimensionless form

$$i\frac{\partial u}{\partial s} + \left(\frac{\partial^2}{\partial\xi^2} + \frac{\partial^2}{\partial\eta^2}\right)u + \frac{c_1 u}{1+c_2|u|^2} + c_3|v|^2 u + c_4 w u = 0, \quad (7)$$

where $s = z/L_{\text{diff}}$, $(\xi, \eta) = (x, y)/R_{\perp}$, $u = \Omega_p/U_0$, $v = E_0(x, y)/V_0$, and $w = B_1(x, y)/W_0$, with $L_{\text{diff}} (\equiv 2R_{\perp}^2\omega_p/c)$, R_{\perp} , U_0 , V_0 , and W_0 being, respectively, characteristic diffraction length, beam radius, half Rabi frequency of the probe field, intensity of the far-detuned (Stark) optical lattice field, and intensity of the magnetic field. The coefficients in Eq. (7) are given by $c_1 = \kappa_{13}d_2L_{\text{diff}}/D$, $c_2 = WU_0^2$, $c_3 = \alpha L_{\text{diff}}V_0^2$, and $c_4 = \beta L_{\text{diff}}W_0$.

For a practical example, we select the D_1 line transition $5^2S_{1/2} \rightarrow 5^2P_{1/2}$ of ^{87}Rb atoms. The levels of the system are taken as $|1\rangle = |5S_{1/2}, F=1, m_F=-1\rangle$, $|2\rangle = |5S_{1/2}, F=2, m_F=-1\rangle$, $|3\rangle = |5P_{1/2}, F=2, m_F=-2\rangle$. The parameters are $\gamma_1 = \Delta_1 = 0$, $2\gamma_2 = 300 \text{ s}^{-1}$, $2\gamma_3 = 3.6 \times 10^7 \text{ s}^{-1}$, $\omega_p = 2.37 \times 10^{15} \text{ s}^{-1}$, and $R_x = 2.52 \times 10^{-3} \text{ cm}$ [41]. According to the formulas below Eq. (7), and taking $\Omega_c = 6.0 \times 10^7 \text{ s}^{-1}$, $\kappa_{13} = 1.0 \times 10^{11} \text{ cm}^{-1} \text{ s}^{-1}$, $\Delta_1 = 0$, $\Delta_2 = 3.6 \times 10^4 \text{ s}^{-1}$, $\Delta_3 = 1.0 \times 10^9 \text{ s}^{-1}$, $U_0 = 6.0 \times 10^7 \sqrt{\sigma_2} \text{ s}^{-1}$, $V_0 = 380\sigma_3 \text{ V/cm}$, and $W_0 = 0.09\sigma_4 \text{ Gs}$, $\sigma_{1,2,3,4}$ are the free parameters that can be adjusted by the detuning and the field intensity. Substituting these parameters into the coefficient expressions of the SNLSE (7), we can obtain the typical diffraction length $L_{\text{diff}} = 1.0 \text{ cm}$, and

$$c_1/\sigma_1 = 1.0 + 0.01i, \quad c_2/\sigma_2 = 1.0, \quad (8a)$$

$$c_3/\sigma_3 = 1.0 + 0.001i, \quad c_4/\sigma_4 = 1.0 + 0.001i. \quad (8b)$$

According to the above results, the imaginary parts of σ_i ($i = 1-4$) can be neglected. Therefore, Eq. (7) can be written as

$$i\frac{\partial u}{\partial s} + \left(\frac{\partial^2}{\partial\xi^2} + \frac{\partial^2}{\partial\eta^2}\right)u + \frac{\sigma_1 u}{1+\sigma_2|u|^2} + \sigma_3|v|^2 u + \sigma_4 w u = 0, \quad (9)$$

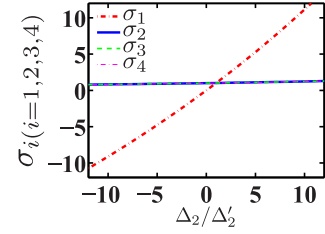


FIG. 2. Curves of coefficients σ_i ($i = 1$ to 4) with the detuning Δ_2/Δ'_2 . The parameters are shown as above, and $\Delta'_2 = 3.6 \times 10^4 \text{ s}^{-1}$.

where the size and sign of σ_1 , σ_2 , σ_3 , and σ_4 can be controlled by Δ_2 , U_0 , V_0 , and W_0 , respectively. From the coefficient expressions below Eq. (6), we find that σ_{1-4} relate to Δ_2 , but the effect of Δ_2 on $\sigma_{2,3,4}$ can be ignored as shown in Fig. 2. Thus, these coefficients can be controlled individually by the system parameters. Thus, we obtain the (2+1)D SNLSE (9) with the trapping potential, and the nonlinear coefficient and the intensity of the trapping potential can be adjusted at will.

IV. SOLITON SOLUTIONS AND THEIR PROPERTIES

In this section, we discuss the soliton solutions of Eq. (9), their properties, and their stability. First, we assume there is the plane-wave solution $u = \psi_0 \exp(i\beta s)$ for Eq. (9); then we obtain

$$u_0 = \sqrt{\frac{\sigma_1 - \beta}{\beta\sigma_2}}, \quad (10)$$

where we take $\sigma_3 = \sigma_4 = 0$. According to Eq. (10), we may find the soliton with uniform background by taking $\sigma_1/\beta \geq 1$ when $\beta\sigma_2 > 0$.

In the linear case, we suppose $u = \psi(\xi, \eta) \exp(i\lambda' s)$, and Eq. (9) becomes the eigenvalue problem

$$\left[\left(\frac{\partial^2}{\partial\xi^2} + \frac{\partial^2}{\partial\eta^2}\right) + \sigma_3|v|^2\right]\psi = \lambda'\psi, \quad (11)$$

where we have taken $\sigma_1 = \sigma_4 = 0$. After taking $|v|^2 = e^{-\frac{\xi^2 + \eta^2}{25}}$, we obtain the curves of eigenvalue spectrums as a function of σ_3 shown in Fig. 15. In Fig. 15(a), the shaded regions denote the spectra for continuous eigenvalues. And with the changing of σ_3 , we plot 12 spectrum lines l_1-l_9 and $l'_1-l'_3$, their eigenfunctions for discrete eigenvalues are shown in Figs. 15(b)–15(m).

On the other hand, considering the nonlinear terms and taking $u = \psi(\xi, \eta) \exp(i\beta s)$, where β is the propagation constant, Eq. (9) becomes

$$-\beta\psi + \left(\frac{\partial^2}{\partial\xi^2} + \frac{\partial^2}{\partial\eta^2}\right)\psi + \frac{\sigma_1\psi}{1+\sigma_2|\psi|^2} + \sigma_3|v|^2\psi + \sigma_4 w \psi = 0. \quad (12)$$

Now, we consider a rough approximation; that is, substituting Eq. (11) into Eq. (12), we obtain

$$\lambda\psi - \beta\psi + \frac{\sigma_1\psi}{1+\sigma_2|\psi|^2} = 0, \quad (13)$$

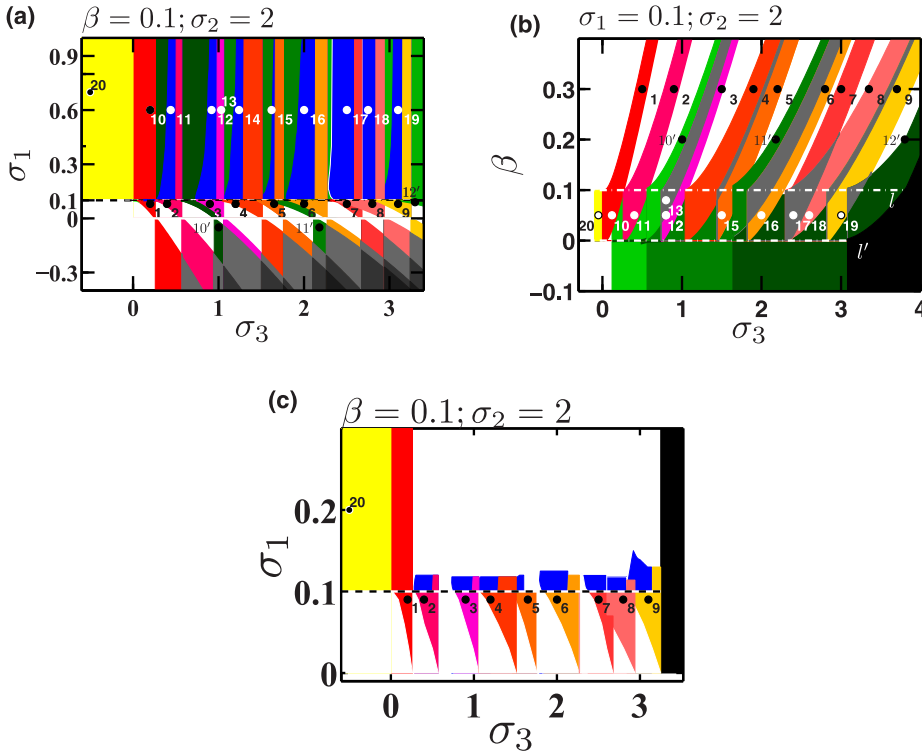


FIG. 3. (a) Existence intervals of various solitons as a function of σ_1 and σ_3 . (b) Existence intervals of various solitons as a function of β and σ_3 . (c) Stability intervals of various solitons shown in panel (a) as a function of σ_1 and σ_3 . In panel (a), the different color shaded regions are used to distinguish the types of nonlinear modes. Here, we use the numbers 1–20 and 10′–12′ to denote the types of nonlinear modes. For example, the number 1 in the interval of $\sigma_1 < 0.1$ and 10 in the interval of $\sigma_1 > 0.1$ denote the bright ground soliton and the bright soliton with the uniform background in the red region, respectively. There are various coexisting nonlinear modes in the gray shaded regions. In panel (b), the same numbers 1–20 and 10′–12′ are used to denote the same type of nonlinear modes as in panel (a).

where $\sigma_4 = 0$, and then

$$\beta - \lambda = \frac{\sigma_1}{1 + \sigma_2 |\psi|^2}. \quad (14)$$

From this formula, we find the existing region of soliton solutions:

$$\sigma_1 > \beta - \lambda > 0, \text{ or } \beta < \sigma_1 + \lambda, \text{ if } \beta > \lambda, \quad (15a)$$

$$\sigma_1 < \beta - \lambda < 0, \text{ or } \beta > \sigma_1 + \lambda, \text{ if } \beta < \lambda. \quad (15b)$$

By using the the Newton conjugate gradient method [42], the profiles and power $P_n = \int_{-\infty}^{+\infty} |\psi|^2 d\xi d\eta$ or the renormalized power $P_n - P_n^0 = \int_{-\infty}^{+\infty} (|\psi|^2 - |\psi_0|^2) d\xi d\eta$ (mainly for the soliton with background) of the soliton solutions are obtained in the following sections, where ψ_0 is the amplitude of the background. Once the soliton solutions ψ are obtained, one can analyze their stability by considering a perturbation to them, i.e.,

$$u = \{\psi + \epsilon[w_0(\xi, \eta)e^{-\lambda s} + v_0^*(\xi, \eta)e^{-\lambda^* s}]\}e^{i\beta s}, \quad (16)$$

where w_0 and v_0 are the normal modes, and λ is the corresponding eigenvalue of the perturbation. Substituting Eq. (16) into Eq. (9), one obtains the following linear eigenvalue problem:

$$\begin{pmatrix} L_1 & L_2 \\ -L_2^* & -L_1 \end{pmatrix} \begin{pmatrix} w_0 \\ v_0 \end{pmatrix} = i\lambda \begin{pmatrix} w_0 \\ v_0 \end{pmatrix}, \quad (17)$$

with $L_1 = -\beta + \nabla_{\perp}^2 + \frac{\sigma_1}{1 + \sigma_2 |\psi|^2} - \frac{\sigma_1 |\psi|^2}{(1 + \sigma_2 |\psi|^2)^2} + \sigma_3 |v|^2 + \sigma_4 w$ and $L_2 = -\frac{\sigma_1 \psi^2}{(1 + \sigma_2 |\psi|^2)^2}$, which can be solved numerically by using the Fourier collocation method [42]. The soliton solutions ψ are stable if the real parts of all the eigenvalues are

positive or zero. We also prove their stability by the split-step Fourier propagation method.

A. Soliton solutions with Gaussian potential

We now present the soliton solutions of Eq. (12) with $\sigma_2 = 2$ and $\sigma_4 = 0$, and check their stability by using the numerical simulations. Here we take the trapping potential $|v|^2 = e^{-\frac{\xi^2 + \eta^2}{25}}$.

We show bright soliton and higher-order defect mode solutions of Eq. (12) in different parameter intervals of σ_1 and σ_3 . After choosing the propagation constant $\beta = 0.1$ or nonlinear coefficient $\sigma_1 = 0.1$, we obtain the existence and stability regions of various solitons, shown in Fig. 3. In Figs. 3(a) and 3(b), the phase diagrams of soliton types are shown. The different color shaded regions marked by the numbers 1–20 and 10′–12′ are used to distinguish the different types of nonlinear modes. For example, in the red region of Fig. 3(a), the number 1 in the interval of $\sigma_1 < 0.1$ and the number 10 in the interval of $\sigma_1 > 0.1$ denote the bright ground soliton shown in Fig. 4(a1) and the bright soliton with the uniform background shown in Fig. 4(a10), respectively. There are various coexisting nonlinear modes in the gray shaded regions. The same numbers 1–20 and 10′–12′ in Fig. 3(b) denote the same type of nonlinear modes as shown in Fig. 3(a). The profiles of nonlinear modes will be shown in the following figures. After taking $\beta = 0.1$, $\sigma_2 = 2$, we show two curves of phase transition for the types of nonlinear modes $\sigma_3 = 0$ and $\sigma_1 = 0.1$ in Fig. 3(a). However, not all these nonlinear modes in Fig. 3(a) are stable; we show the stable intervals in Fig. 3(c). Through Fig. 3(c), we know there are stable regions for every kind of nonlinear mode in Fig. 3(a).

In Fig. 4, the profiles of solitons are shown. From Figs. 4(a1)–4(a9), if we fix $\sigma_1 = 0.09$ ($\sigma_1 < \beta$), the number of

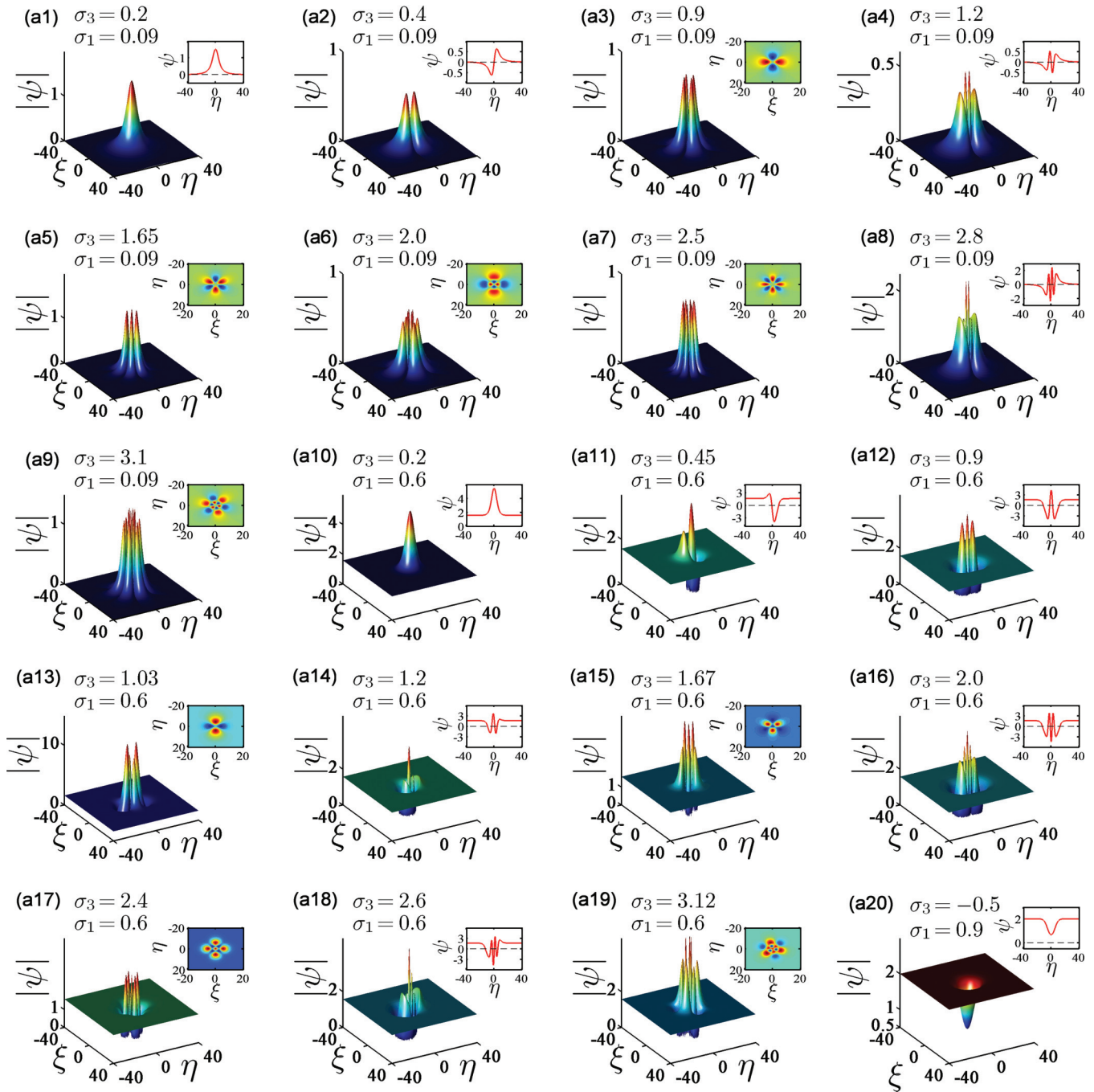


FIG. 4. (a1–a20) Profiles $|\psi|$ of various solitons, with corresponding parameters marked by the dots (or numbers 1–20) in Figs. 3(a) and 3(b). There are the ground solitons, dipole solitons, quadrupole solitons, and multipole solitons with and without uniform background, which we call the multipole solitons and the multipole defect modes. Insets: Profiles ψ by taking $\xi = 0$ or the two-dimensional projection.

peaks will increase with σ_3 . The profiles of the ground soliton, the dipole soliton, the ring quadrupole soliton, the linear-quadrupole soliton along the η direction, the ring sextupole soliton (consisting of six peaks), the dual ring octupole soliton (consisting of eight peaks), the single ring octupole soliton, the linear-sextupole soliton along the η direction, and the dual ring 12-pole soliton (consisting of 12 peaks) are shown in Figs. 4(a1)–4(a9), respectively. These ring-type solitons were also called “necklace” solitons [43].

After changing σ_1 into 0.6 ($\sigma_1 > \beta$), a uniform background will appear in the soliton profiles. The bright ground soliton

in Fig. 4(a1) becomes the bright soliton with uniform background as shown in Fig. 4(a10), but the multipole solitons in Figs. 4(a2)–4(a9) become higher-order defect modes as shown in Figs. 4(a11)–4(a19), in which there are many peaks, so we call them the multipole defect modes. By comparing Fig. 4(a3) with Figs. 4(a12) and 4(a13), we find the ring quadrupole soliton will become two kinds of defect mode denoted by two colors. Because the profiles in Figs. 4(a3) and 4(a13) have similarity except for the uniform background, the same color is used. After taking $\sigma_3 < 0$, we find another defect mode shown in Fig. 4(a20). In general, the bright soliton and dark soliton are

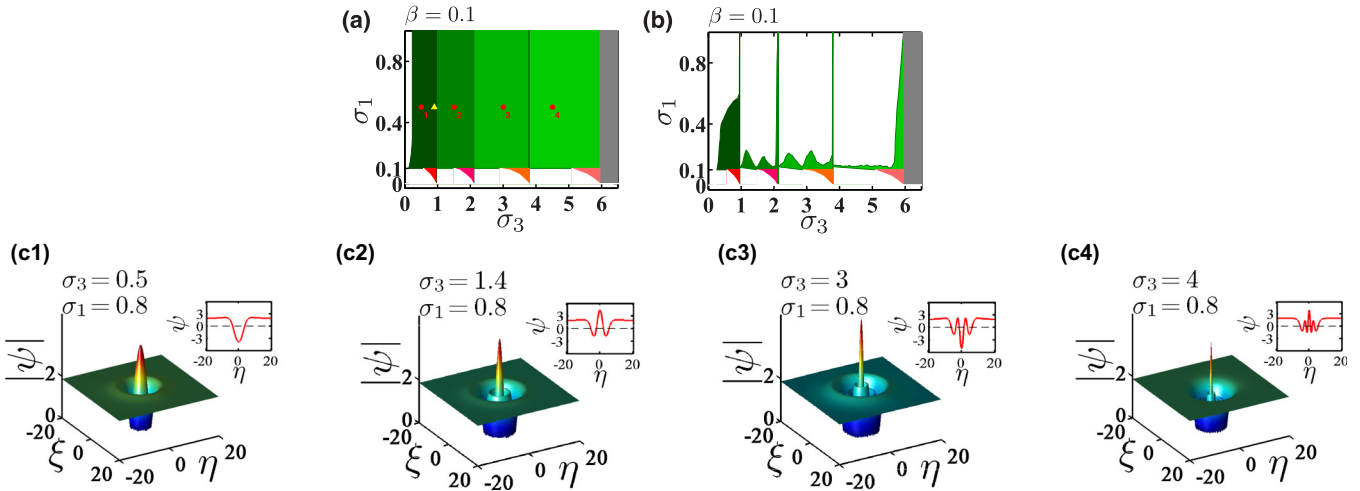


FIG. 5. (a, b) Existence and stability intervals of various uniform ring defect modes as a function of σ_1 and σ_3 , respectively. (c1–c4) Profiles of various ring solitons, with corresponding parameters marked by the dots in panel (a). There are the single-ring defect modes, the binary-ring defect modes, the ternary-ring defect modes, and the quaternary-ring defect modes. Insets: Profiles by taking $\xi = 0$. In panel (a), the numbers 1–4 are used to denote the type of nonlinear modes. In the regions of $\sigma_1 < 0.1$, all these existence solitons do not have the uniform background.

determined by the nonlinearity of self-focusing or defocusing. However, the type of soliton is determined by the sign of the trapping potential in our scheme.

Through the phase diagram shown in Figs. 3(a) and 3(b), we not only find two distinct phase transition points $\sigma_1 = 0.1$ between the bright and the defect mode and $\sigma_3 = 0$ between two kinds of higher-order modes, but we also define the existence range of the defect mode. After some further numerical experiments, we find that the height of the uniform background will increase with σ_1 , and the phase transition point $\sigma_1 = 0.1$ is related to β_1 , $\sigma_1/\beta = 1$ as shown in Eq. (10), which will be shown in the following figures. From Fig. 3(c), we find that most of the solitons shown in Figs. 3(a) and 3(b) are stable. These results for $\sigma_3 > 3.25$ will also be shown below.

In the same parameter region as in Fig. 3(a), there are other types of solitons. By further numerical calculation, we find

uniform ring defect modes as shown in Fig. 5 other than the “necklace-ring” multipole solitons as shown in Fig. 4.

In Fig. 5(a), the phase diagram of the bright soliton and defect mode with different ring numbers are shown. We also prove that all of the ring bright solitons and the ring defect modes are stable in some existence regions by Fig. 5(b). In Fig. 5(a), the numbers 1–4 are used to denote the type of nonlinear mode. In the regions of $\sigma_1 < 0.1$, all the existence solitons do not have the uniform background. From Figs. 5(c1)–5(c4), we show the single-ring defect mode, the binary-ring defect mode, the ternary-ring defect mode, and the quaternary-ring defect mode, in which there are one, two, three, and four extreme value rings shown by the peak value of these insets, respectively. Additionally, the number of rings increases with σ_3 .

The above results illustrate that the profiles of solitons are related to the parameters σ_1 , σ_3 , and β . Through these results

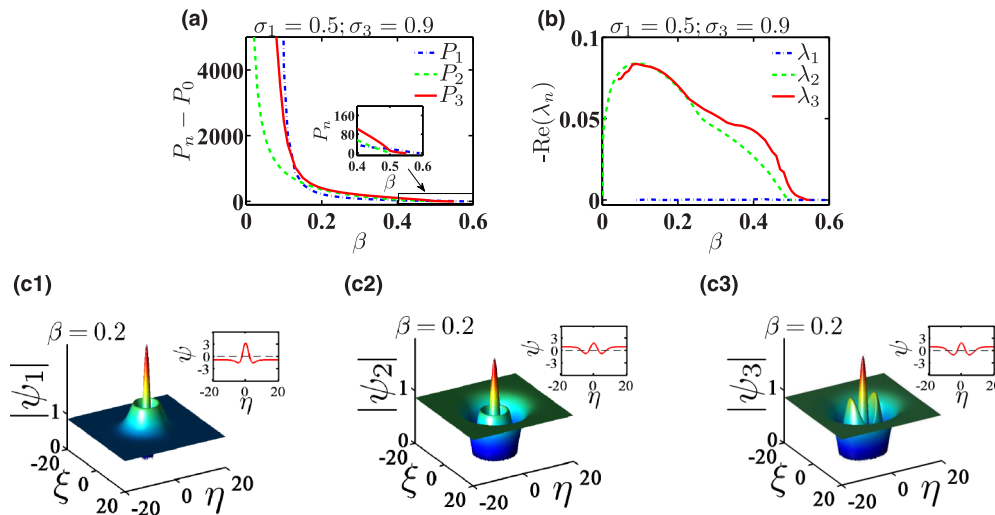


FIG. 6. (a, b) Power and stability curves of three types of the ring defect modes as a function of β . (c1–c3) Profiles of these ring solitons. The corresponding parameters are also marked by the (yellow) triangles in Fig. 5(a). The inset in panel (a) shows the detail. The insets in panels (c1)–(c3) show the profiles by taking $\xi = 0$.

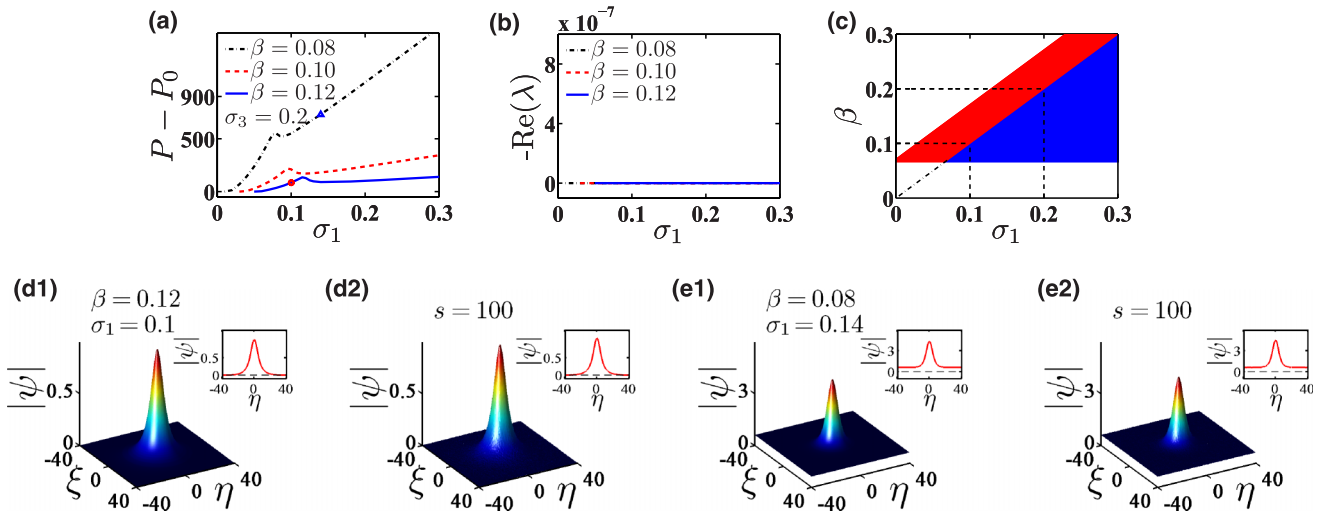


FIG. 7. (a, b) Renormalized power and stability curves of the ground solitons as a function of σ_1 . (c) Phase diagram between the ground soliton without and with the uniform background as a function of β and σ_1 . The red (blue) region is used to denote the existence regions of the bright soliton without (with) the uniform background. (d1, d2) Profile of the ground soliton by taking $\beta = 0.12$, $\sigma_1 = 0.1$ and the evolution results of the ground soliton in the presence of the random perturbation by simulating Eq. (9). (e1, e2) Analogous results as shown in panels (d1) and (d2) with $\beta = 0.08$, $\sigma_1 = 0.14$. Insets: Profiles by taking $\xi = 0$.

shown in Fig. 5(a), even if the parameters σ_1 , σ_3 , and β are fixed as marked by the (yellow) triangles, there still exist two types of solitons. We need to know whether there are other types of solitons. By numerical search, we find three kinds of solitons as shown in Fig. 6 when we take $\sigma_1 = 0.5$ and $\sigma_3 = 0.9$. Figures 6(a) and 6(b) illustrate the power and stability curves as a function of the propagation constant β . From the stability curves, we know that there exist stable solitons in some regions. From Fig. 6(a), when $\beta = 0.2$, the powers of solitons are approximately equal, but their profiles shown in Figs. 6(c1)–6(c3) are entirely different.

From the above results, we know that the types of solitons are diverse. Furthermore, the relationship between the prop-

agation constant β and the phase transition point about σ_1 is also worth proving further. We choose the ground soliton without and with uniform background, the ring bright soliton and the ring defect mode, the ring multipole bright soliton and the ring multipole defect mode, and the higher-order defect mode to discuss their properties and the effect of β on the phase transition point about σ_1 .

In Fig. 7, we show the results of the ground soliton without and with uniform background. After choosing $\sigma_3 = 0.2$, we take $\beta = 0.08, 0.10$, and 0.12 , respectively. The power curves in Fig. 7(a) and the stability curves in Fig. 7(b) tell us that all the ground solitons without and with uniform background are stable. In Fig. 7(c), the phase diagram of the ground soliton is

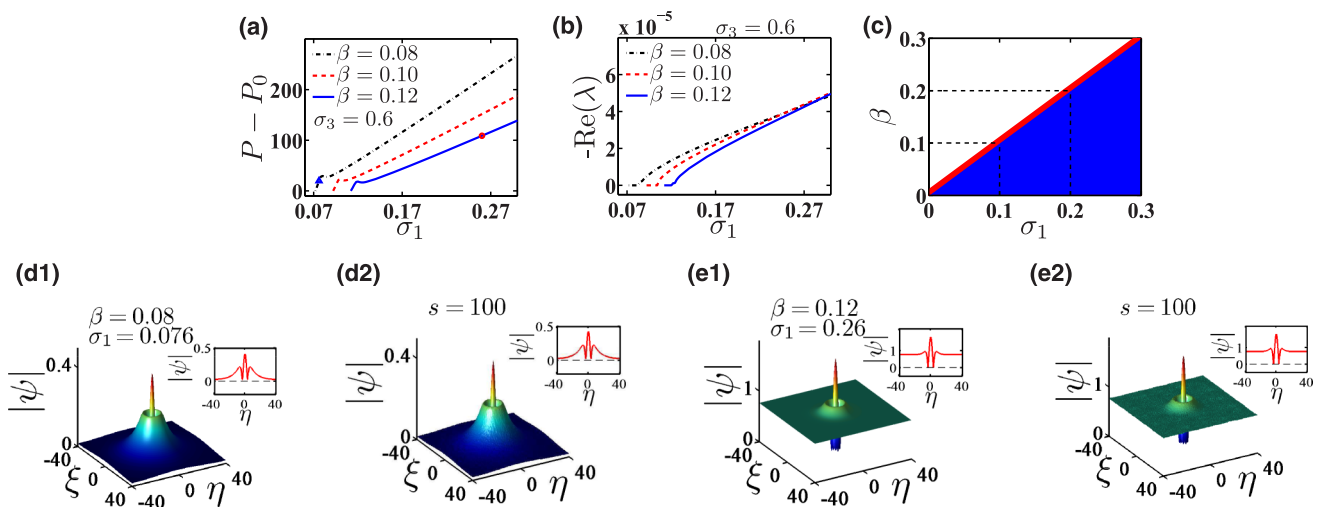


FIG. 8. (a, b) Renormalized power and stability curves of the uniform ring soliton as a function of σ_1 . (c) Phase diagram between the uniform ring bright soliton and the uniform ring defect mode as a function of β and σ_1 . The red (blue) region is used to denote the existence regions of the ring bright soliton (the ring defect mode with the uniform background). (d1, d2) Profile of the uniform ring bright soliton by taking $\beta = 0.08$, $\sigma_1 = 0.076$ and the evolution results of the uniform ring bright soliton in the presence of the random perturbation by simulating Eq. (9). (e1, e2) Analogous results as shown in panels (d1) and (d2) with $\beta = 0.12$, $\sigma_1 = 0.26$. Insets: Profiles by taking $\xi = 0$.

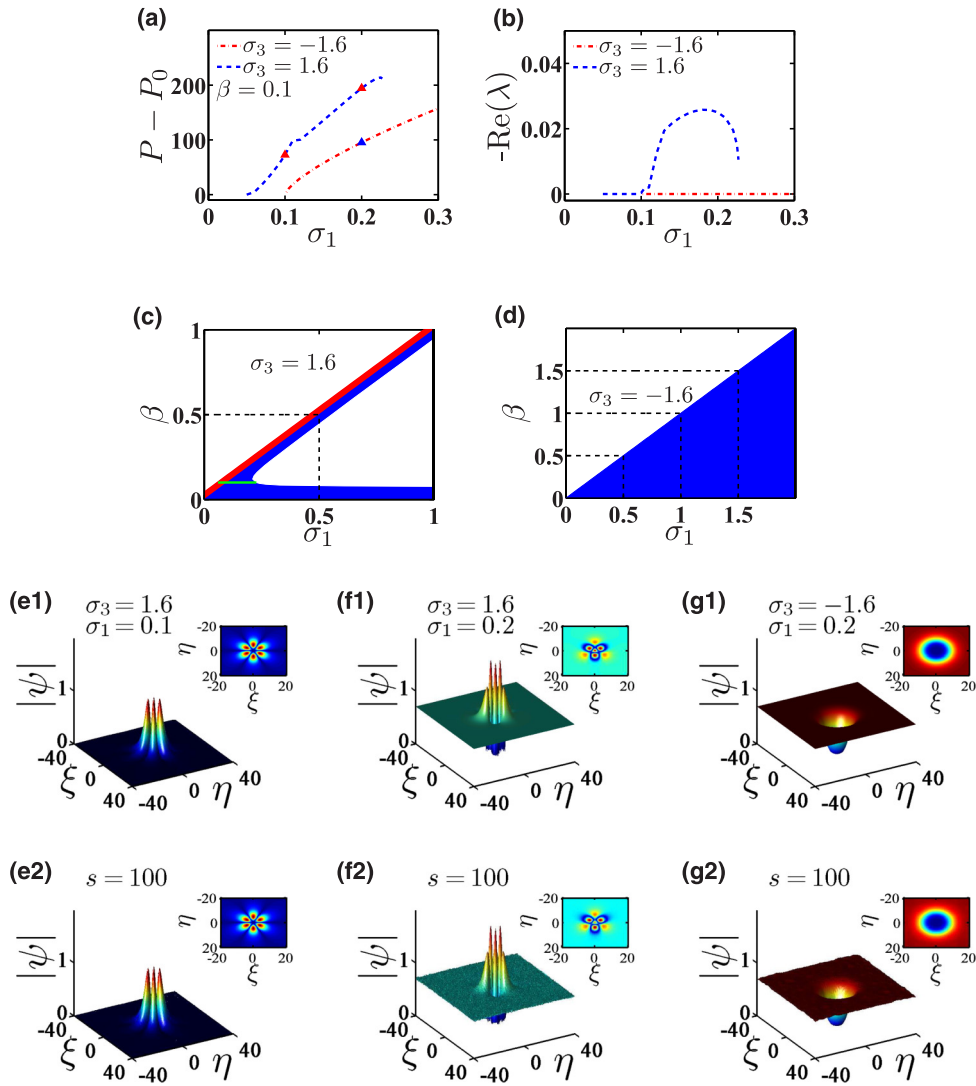


FIG. 9. (a, b) Renormalized power and stability curves of the ring multipole soliton and defect mode as a function of σ_1 . (c) Phase diagram between the ring multipole bright soliton and the ring multipole defect mode as a function of β and σ_1 . The red (blue) region is used to denote the existence regions of the ring multipole soliton (the ring multipole defect mode with the uniform background). (d) Existence regions of the defect mode as a function of β and σ_1 . The blue region denotes the existence regions of the higher-order defect mode with the uniform background. (e1, f1, g1) Profiles of various solitons marked by the triangles in panel (a). (e2, f2, g2) Evolution results for various solitons in panels (e1), (f1), and (g1), respectively. Insets: Two-dimensional projections of the profiles $|\psi|$.

shown. The red regions denote the ground solitons without uniform background, the blue regions denote the ground solitons with uniform background, and the blank regions denote that there is no ground soliton. It is obvious that the straight line $\beta = \sigma_1$ is the boundary of two types of the ground solitons. If we carefully observe Figs. 7(a) and 7(c), the first turning point of every power curve is the phase transition point just right. In Fig. 7(d1), we plot the profile of the ground soliton; its parameters are marked by the small (red) dot in Fig. 7(a). Its stability is proved further by a numerical propagation of Eq. (9), and adding the random perturbations into them, i.e., we take $u(s = 0, \xi, \eta) = \psi(1 + \varepsilon f)$, where $\varepsilon = 0.1$, f is a random variable uniformly distributed in the interval $[0, 1]$. The evolution results are shown in Fig. 7(d2). The analogous results taking the parameters $\beta = 0.08$ and $\sigma_1 = 0.14$ marked by the (blue) triangle are shown in Figs. 7(e1) and 7(e2).

The results for the uniform ring bright soliton and the uniform ring defect mode are shown in Fig. 8. As in Fig. 7, the renormalized power and stability curves are shown in Figs. 8(a) and 8(b). The strictly stable regions correspond to the regions in front of the first turning point of the power curve. In Fig. 8(c), the phase diagrams for the uniform ring bright and defect modes are drawn, and the straight line $\beta = \sigma_1$ is the boundary of two phases. The conclusion that the first turning point of the power curve is the phase transition point also holds. In Figs. 8(d1) and 8(d2), the corresponding soliton profile marked by the (blue) triangle in Fig. 8(a) and its evolution results are shown. Taking the soliton marked by the (red) dot in Fig. 8(a), though the uniform ring defect mode shown in Fig. 8(e1) is unstable according to Fig. 8(b), the numerical evolution in Fig. 8(e2) tells us that the soliton profile is still conserved after propagating 100 cm.

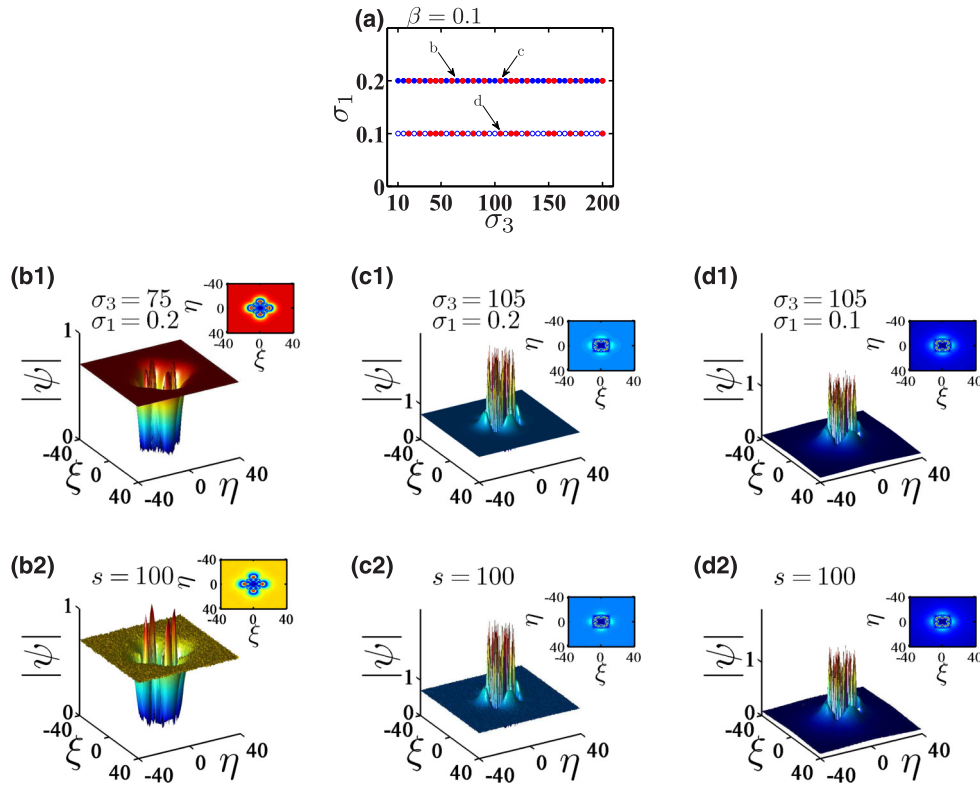


FIG. 10. (a) Existence and stability regions for the soliton as a function of σ_1 and σ_3 with $\beta = 0.1$. The solid (blue) dots marked by letter *b* denote that there exist unstable solitons; the solid (red) dots marked by letters *c* and *d* denote that there exist stable solitons; the circles denote that there are no solitons. Of course, we only choose $\sigma_1 = 0.1$ and 0.2 . (b1, c1, d1) Profiles of multipole solitons marked by letters *b*, *c*, and *d* in panel (a). (b2, c2, d2) Evolution results for various solitons in panels (b1), (c1), and (d1), respectively. Insets: Two-dimensional projections of the profiles $|\psi|$.

We now investigate whether the above conclusions are suitable for the multipole solitons and higher-order defect modes. In Fig. 9, we take $\beta_1 = 0.1$ and $\sigma_3 = \pm 1.6$ as examples. The renormalized power and stability curves are shown in Figs. 9(a) and 9(b). We find that the ring multipole bright soliton is stable, but the stability region of the ring multipole defect mode is very narrow. In Fig. 9(c), the phase diagrams

for the ring multipole bright solitons and defect modes are drawn, and the straight line $\beta = \sigma_1$ is still the boundary of two phases. The phase diagram for the existence of the higher-order defect mode is shown in Fig. 9(d), in which the higher-order defect mode only exists in the regions of $\sigma_1 \geq \beta$. In Figs. 9(e1), 9(f1), and 9(g1), the corresponding soliton profiles marked by the triangle in Fig. 9(a) are shown. Taking these solitons

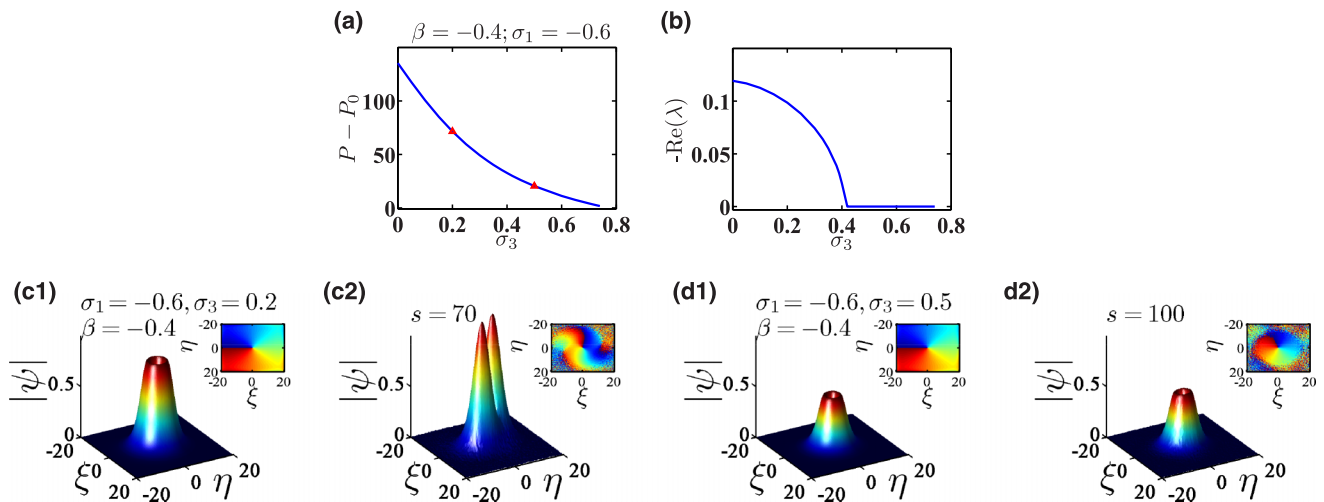


FIG. 11. (a, b) Power and stability curves of vortices as a function of σ_3 . (c1, c2, d1, d2) Profiles and evolution results of these vortices marked by the (red) triangle in panel (a). Insets: Phases.

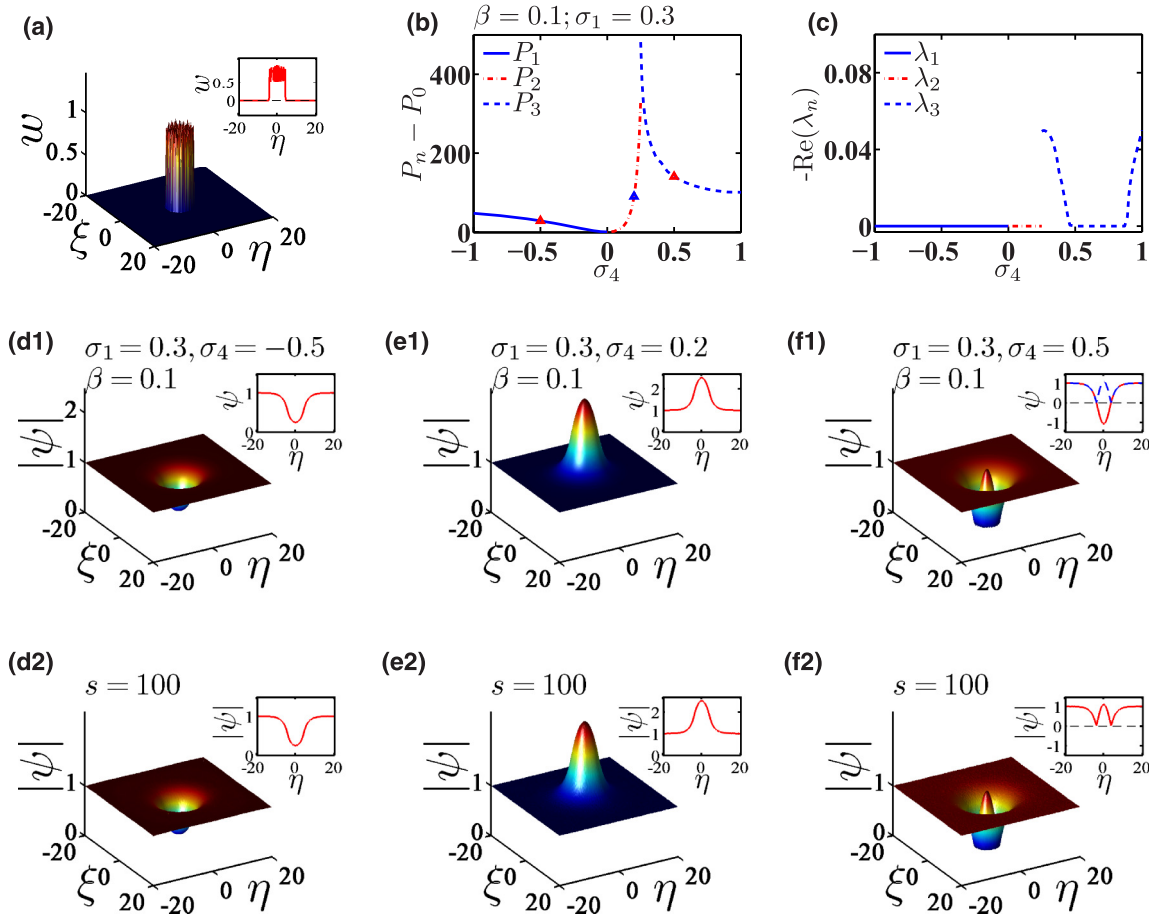


FIG. 12. (a) Profile of the random potential provided by the random magnetic field. (b, c) Power and stability curves for the dark solitons, the ground solitons with the uniform background, and the darklike solitons as a function of σ_4 . (d1, e1, f1) Profiles of various solitons marked by the triangles in panel (a). (d2, e2, f2) Evolution results for various solitons in panels (e1), (f1), and (g1), respectively. Insets: Profiles by taking $\xi = 0$. In the inset of panel (f1), the (blue) dashed line denotes the profile $|\psi|$, which can be used to compare with the evolution results conveniently.

as the initial values, and adding the random perturbations into them, the numerical propagation results of Eq. (9) are shown in Figs. 9(e2), 9(f2), and 9(g2), which tell us that these soliton profiles are still conserved after propagating 100 cm, except that there are some small perturbations appearing in the background of the multipole defect mode shown in Fig. 9(f2).

Through the above three figures, we conclude that the boundary of the phase transition is $\beta = \sigma_1$, which is consistent with the theoretical analysis. Solitons such as the higher-order defect mode, the ground soliton, and the multipole soliton can transform continuously by controlling the parameters σ_1 and σ_3 . From Fig. 3, we know that the number of peaks in every multipole soliton will increase with σ_3 . When σ_3 is increased further, we find some interesting results.

In Fig. 10, we show the results of $5 < \sigma_3 < 200$ after choosing $\beta = 0.1$ and $\sigma_1 = 0.1$ or 0.2 . The phase diagram of σ_1 and σ_3 is shown in Fig. 10(a), in which the solid dots denote that there exist solitons, and the circles denote that there are no solitons. The red (blue) solid dots denote that these solitons are stable (unstable). The solitons marked by the letters *b*, *c*, and *d* in Fig. 10(a) are shown in Figs. 10(b1), 10(c1), and 10(d1). Their propagation results are shown in Figs. 10(b2), 10(c2), and 10(d2). We can observe clearly that the defect mode

in Fig. 10(b1) is unstable through the insets in Figs. 10(b1) and 10(b2). The conclusion that the number of peaks in the multipole soliton increases with σ_3 still holds.

In this scheme, we have found diverse solitons. We now investigate whether there are stable vortices. After some numerical experiments, we find that when the propagation constants β and σ_1 are both less than zero there exist vortices. Taking $\beta = -0.4$ and $\sigma_1 = -0.6$, we show the power and stability curves as a function of σ_3 in Figs. 11(a) and 11(b). With the increasing of σ_3 , the vortices will become stable. That is, we can obtain the stable vortices by adding a Gaussian trapping potential in our scheme. In Figs. 11(c1) and 11(d1), two vortices are shown. However, after propagating 70 cm, the unstable vortex breaks down into two solitons as shown in Fig. 11(c2); in contrast, the profile and phase of the stable vortex will remain the same after propagating 100 cm as shown in Fig. 11(d2).

B. Soliton solutions with random potential

It is known that there are not stable high-dimensional solitons and vortices in the SNLSE without trapping potential except for the ground soliton. In the above subsection, the Gaussian potential can be used to stabilize the high-

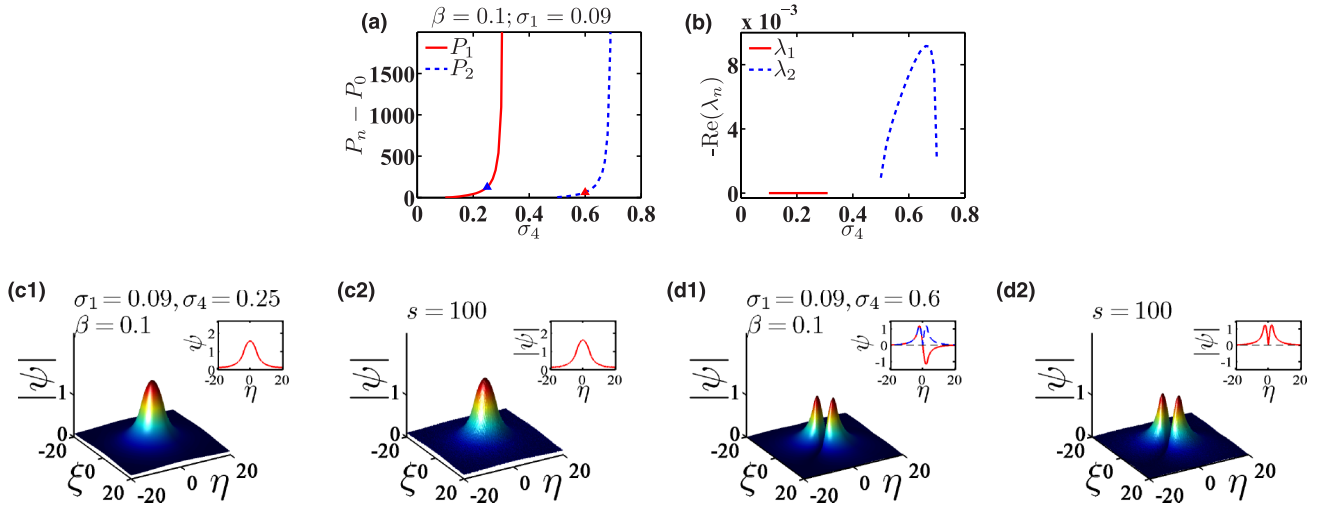


FIG. 13. (a, b) Power and stability curves for the ground and dipole solitons as a function of σ_4 . (c1, c2, d1, d2) Profiles and evolution results of the ground soliton marked by the (blue) triangle in panel (a) and the dipole soliton marked by the (red) triangle in panel (a). Insets: Profiles by taking $\xi = 0$. In the inset of panel (d1), the (red) solid line clearly denotes the profile of the dipole soliton, and the (blue) dashed line can be used to compare with the evolution results conveniently.

dimensional solitons and vortices. It is also worth exploring whether there are other simple projects to stabilize these nonlinear solutions. Because the random potential is easy to design and appears inevitably in the experimental scheme, we now investigate whether the random potential can be used to stabilize solitons and vortices. In our scheme, the random potential can be realized by taking $|v|^2 = \rho(\xi, \eta)$, which can be designed by laser speckles [44], or taking $w = \rho(\xi, \eta)$, which can be designed by adding a demagnetized neodymium-iron-boron ferromagnet [40], where ρ is a random variable. It is well known that the random potential contributes to the localization of the linear eigenstate in the linear model. We need to know how it effects the solitons and vortices in the SNLSE.

In this subsection, we take $\sigma_2 = 2$, $\sigma_3 = 0$, and $w = 1 - 0.5\rho(\xi, \eta)$, where ρ is a random variable uniformly distributed in the interval $[0,1]$ when $\xi^2 + \eta^2 \leq 5^2$, otherwise $\rho = 0$.

Thus, the widths of the random and the Gaussian potential are the same.

In Fig. 12(a), the profile of the trapping potential is shown. After fixing $\beta = 0.1$ and $\sigma_1 = 0.3$, we obtain the power and stability curves as shown in Figs. 12(b) and 12(c). With σ_3 from -1 to 1 , the graylike soliton, the ground soliton with uniform background, and the darklike soliton are found, and all of them are stable in some regions as shown in Fig. 12(c). Their profiles marked by the triangles in Fig. 12(b) are shown in Figs. 12(d1), 12(e1), and 12(f1). Taking them as the initial values, and adding the random perturbations, we obtain the evolution results after propagating 100 cm by numerical simulation of Eq. (9) in Figs. 12(d2), 12(e2), and 12(f2). Through these results, the stability of solitons is proved further. From the above results, we conclude that the random potential can be used to stabilize the soliton. However, the random potential

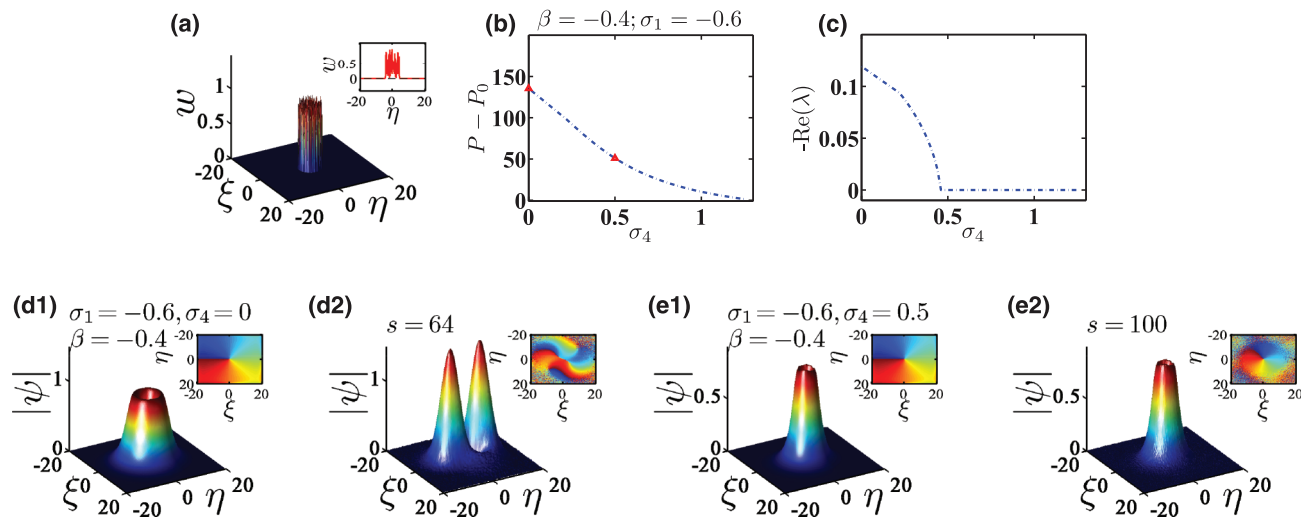


FIG. 14. (a) Profile of the random potential provided by the random magnetic field. (b, c) Power and stability curves of vortices as a function of σ_4 . (d1, d2, e1, e2) Profiles and evolution results of these vortices marked by the (red) triangle in panel (a). Insets: Phases.

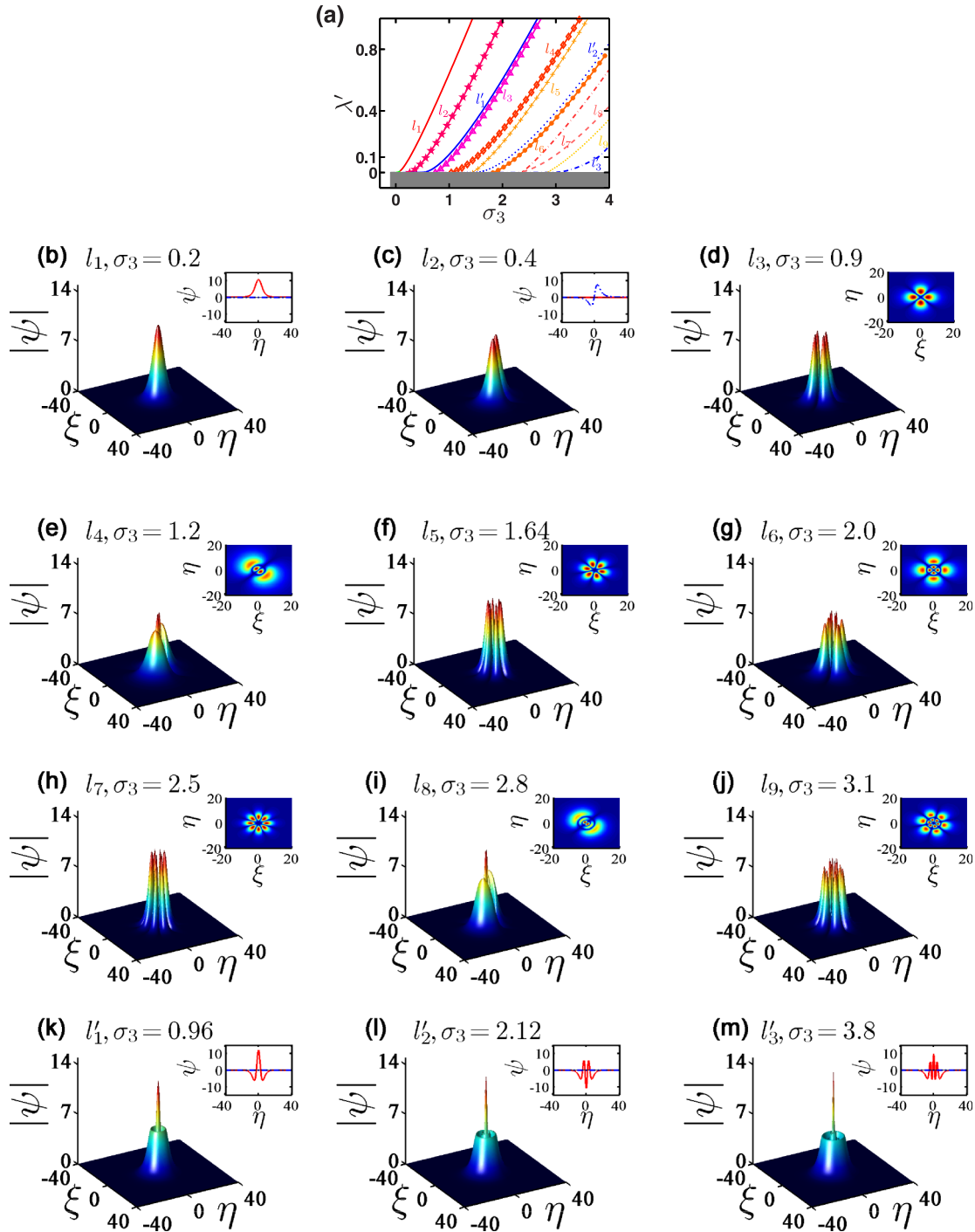


FIG. 15. (a) Eigenvalue spectrum of Eq. (11) as a function of σ_3 . (b–m) Eigenfunctions corresponding to the eigenvalue spectrum.

destroys the symmetry of the trapping potential, and the ring multipole soliton cannot be found.

Under the phase transition point, that is, $\sigma_1 < \beta$, we obtain the ground soliton and the dipole soliton using the same random potential as shown in Fig. 12(a). The power and stability curves are shown in Figs. 13(a) and 13(b). The profile of the ground soliton marked by the (blue) triangle in Fig. 13(a) is shown in Fig. 13(c1), and its stable propagating result is shown in Fig. 13(c2). The dipole soliton is shown in Fig. 13(d1), the (red) solid line of the inset denotes the profile ψ after taking

$\xi = 0$, and the (blue) dashed line of the inset denotes the profile $|\psi|$ after taking $\xi = 0$. The propagating result is shown in Fig. 13(d2). Though the dipole soliton shown in Fig. 13(d1) is unstable through Fig. 13(b), it can retain its profile perfectly after propagating 100 cm as shown in Fig. 13(d2).

Through the above two figures, it is obvious that the random trapping potential can be used to stabilize the soliton. We now investigate whether it can also be used to stabilize the vortices. We find that the simple potential $w = \rho(\xi, \eta)$ shown in Fig. 14(a) is enough to supply the vortices, rather than

the composite potential $w = 1 - 0.5\rho(\xi, \eta)$. In Figs. 14(b) and 14(c), we show the power and stabilized curves for the vortices. There exists the vortex solution even if $\sigma_4 = 0$, but these vortices are all unstable. We find that the stability will strengthen with the random potential increasing. The corresponding profiles marked by the (red) triangle in Fig. 14(a) are shown in Figs. 14(d1) and 14(e1). By the numerical propagating results in Figs. 14(d2) and 14(e2), we find that the unstable vortex will break down into two solitons, but the stable one retains its profile and phase after propagating 100 cm.

V. SUMMARY

In this paper, we have proposed a scheme to design the SNLSE in an active optical medium via EIT. The system we considered was an ensemble of resonant, lifetime-broadened Λ three-level atoms. By the use of the EIT effect induced by a cw control field, the absorption of a probe field was largely suppressed. The envelope equation of the probe field was depicted by a (2+1)D SNLSE with trapping potentials, which include the Gaussian and random potentials. The Gaussian and random potentials were provided by the far-detuned laser field and the random magnetic field, respectively. In this model, we not only found diverse solitons—i.e., the ground soliton with and without uniform background, the ring multipole soliton, the linear-multipole soliton, the multipole defect mode, the higher-order defect mode, the uniform multiring soliton, and the vortex, which resulted from the potential—but also identified the boundary of the phase transition between the bright soliton and the defect mode. In addition, the effect of random potential on the stability of the soliton was also studied,

and we found that the random potential can be used to stabilize the soliton and vortex. However, the random potential also broke the symmetry of the potential, so we only found some kinds of solitons. The results presented here may be useful for understanding the physical properties of coherent atomic systems and guiding experimental study of optical solitons, which may have potential applications in optical information processing and transmission.

ACKNOWLEDGMENTS

This paper was supported by the National Natural Science Foundation of China (Grants No. 11574274 and No. 11675146) and the Natural Science Foundation of Zhejiang Province of China (Grants No. LY15A040002 and No. LZ15A050001).

APPENDIX: EIGENVALUE SPECTRA AND EIGENFUNCTIONS IN SEC. IV

The curves of eigenvalue spectra as a function of σ_3 are shown in Fig. 15. The shaded regions denote the spectra for continuous eigenvalues. With the changing of σ_3 , 12 spectrum lines l_1 – l_9 and l'_1 – l'_3 for discrete eigenvalues are shown in Figs. 15(b)–15(m). Nine kinds of eigenfunctions in Figs. 15(b)–15(j) and solitons in Figs. 3(d1)–3(d9) have very similar profiles. Three kinds of eigenfunctions in Figs. 15(k)–15(m) related to lines l'_1 – l'_3 of Fig. 15(a) and solitons without considering uniform background in Figs. 4(c2)–4(c4) also have very similar profiles. Thus, all these solutions without uniform background are just the nonlinear extension of the linear modes.

-
- [1] G. I. Stegeman and M. Segev, *Science* **286**, 1518 (1999).
 - [2] Y. S. Kivshar and G. P. Agrawal, *Optical Solitons: From Fibers to Photonic Crystals* (Academic, New York, 2003).
 - [3] Y. F. Chen, K. Beckwitt, F. W. Wise, and B. A. Malomed, *Phys. Rev. E* **70**, 046610 (2004).
 - [4] B. A. Malomed, D. Mihalache, F. Wise, and L. Torner, *J. Phys. B* **7**, R53 (2005).
 - [5] M. J. Paz-Alonso and H. Michinel, *Phys. Rev. Lett.* **94**, 093901 (2005).
 - [6] S. E. Harris, J. E. Field, and A. Imamoglu, *Phys. Rev. Lett.* **64**, 1107 (1990).
 - [7] S. E. Harris, *Phys. Today* **50**(7), 36 (1997).
 - [8] L. V. Hau, S. E. Harris, Z. Dutton, and C. H. Behroozi, *Nature (London)* **397**, 594 (1999).
 - [9] H. Schmidt and A. Imamoglu, *Opt. Lett.* **21**, 1936 (1996).
 - [10] D. F. Phillips, A. Fleischhauer, A. Mair, R. L. Walsworth, and M. D. Lukin, *Phys. Rev. Lett.* **86**, 783 (2001).
 - [11] Z. Chen, Z. Bai, H.-J. Li, C. Hang, and G. Huang, *Sci. Rep.* **5**, 08211 (2015).
 - [12] D. Petrosyan and M. Fleischhauer, *Phys. Rev. Lett.* **100**, 170501 (2008).
 - [13] R. Santra, E. Arimondo, T. Ido, C. H. Greene, and J. Ye, *Phys. Rev. Lett.* **94**, 173002 (2005).
 - [14] Y. Zhang, A. W. Brown, and M. Xiao, *Phys. Rev. Lett.* **99**, 123603 (2007).
 - [15] A. Joshi and M. Xiao, *J. Mod. Optic.* **57**, 1196 (2010).
 - [16] H.-J. Li, Y.-P. Wu, and G. Huang, *Phys. Rev. A* **84**, 033816 (2011).
 - [17] L. Stegano, *Laser Photon. Rev.* **3**, 243 (2009).
 - [18] J. Cheng and G. Huang, *Phys. Rev. A* **83**, 053847 (2011).
 - [19] H.-J. Li, J.-P. Dou, and G. Huang, *Phys. Rev. A* **89**, 033843 (2014).
 - [20] C. Hang, G. Huang, and V. V. Konotop, *Phys. Rev. Lett.* **110**, 083604 (2013).
 - [21] H.-J. Li, J.-P. Dou, and G. Huang, *Opt. Express* **21**, 32053 (2013).
 - [22] J. Sheng, M. A. Miri, D. N. Christodoulides, and M. Xiao, *Phys. Rev. A* **88**, 041803(R) (2013).
 - [23] J. Sheng, J. Wang, M. A. Miri, D. N. Christodoulides, and M. Xiao, *Opt. Express* **23**, 19777 (2015).
 - [24] Z. Zhang, Y. Zhang, J. Sheng, L. Yang, M. A. Miri, D. N. Christodoulides, B. He, Y. Zhang, and M. Xiao, *Phys. Rev. Lett.* **117**, 123601 (2016).
 - [25] H.-J. Li and K. Zhang, *Phys. Rev. A* **95**, 013829 (2017).
 - [26] C. Hang, G. Huang, and L. Deng, *Phys. Rev. E* **74**, 046601 (2006).
 - [27] H.-J. Li, L. Dong, C. Hang, and G. Huang, *Phys. Rev. A* **83**, 023816 (2011).
 - [28] H. Michinel, M. J. Paz-Alonso, and V. M. Pérez-García, *Phys. Rev. Lett.* **96**, 023903 (2006).
 - [29] V. Tikhonenko, Y. S. Kivshar, V. V. Steblina, and A. A. Zozulya, *J. Opt. Soc. Am. B* **15**, 79 (1998).

- [30] A. Dreischuh, G. G. Paulus, F. Zacher, F. Grasbon, and H. Walther, *Phys. Rev. E* **60**, 6111 (1999).
- [31] J. Yang, *Phys. Rev. E* **66**, 026601 (2002).
- [32] N. K. Efremidis, J. Hudock, D. N. Christodoulides, J. W. Fleischer, O. Cohen, and M. Segev, *Phys. Rev. Lett.* **91**, 213906 (2003).
- [33] J. W. Fleischer, M. Segev, N. K. Efremidis, and D. N. Christodoulides, *Nature (London)* **422**, 147 (2003).
- [34] D. N. Christodoulides and M. I. Carvalho, *J. Opt. Soc. Am. B* **12**, 1628 (1995).
- [35] J. Yang and Z. Chen, *Phys. Rev. E* **73**, 026609 (2006).
- [36] C. Huang, J. Zheng, S. Zhong, and L. Dong, *Opt. Commun.* **284**, 4225 (2011).
- [37] K. Zhan and Z. Li, *Opt. Commun.* **300**, 249 (2013).
- [38] K. Zhan and Z. Li, *Opt. Commun.* **307**, 80 (2013).
- [39] N. K. Efremidis, S. Sears, D. N. Christodoulides, J. W. Fleischer, and M. Segev, *Phys. Rev. E* **66**, 046602 (2002).
- [40] F. B. Mancoff, R. M. Clarke, C. M. Marcus, S. C. Zhang, K. Campman, and A. C. Gossard, *Phys. Rev. B* **51**, 13269 (1995).
- [41] D. A. Steck, Rubidium 87 D Line Data, <http://steck.us/alkalidata/>.
- [42] J. Yang, *Nonlinear Waves in Integrable and Nonintegrable Systems* (SIAM, Philadelphia, 2011).
- [43] M. Soljačić, S. Sears, and M. Segev, *Phys. Rev. Lett.* **81**, 4851 (1998).
- [44] J. E. Lye, L. Fallani, M. Modugno, D. S. Wiersma, C. Fort, and M. Inguscio, *Phys. Rev. Lett.* **95**, 070401 (2005).